RESEARCH ARTICLE

ADVANCED MATERIALS
www.advmat.de

Imitating Architectural Mortise-Tenon Structure for Stable Ni-Rich Layered Cathodes

Xinghua Tan, Zhefeng Chen, Tongchao Liu, Yongxin Zhang, Mingjian Zhang, Shunning Li, Weiguo Chu, Kang Liu, Peihua Yang,* and Feng Pan**

Ni-rich layered oxides are the most promising cathodes for Li-ion batteries, but chemo-mechanical failures during cycling and large first-cycle capacity loss hinder their applications in high-energy batteries. Herein, by introducing spinel-like mortise-tenon structures into the layered phase of $LiNi_{0.8}Co_{0.1}Mn_{0.1}O_2$ (NCM811), the adverse volume variations in cathode materials can be significantly suppressed. Meanwhile, these mortise-tenon structures play the role of the expressway for fast lithium-ion transport, which is substantiated by experiments and calculations. Moreover, the particles with mortise-tenon structures usually terminate with the most stable (003) facet. The new cathode exhibits a discharge capacity of 215 mAh g^{-1} at 0.1 C with an initial Coulombic efficiency of 97.5%, and capacity retention of 82.2% after 1200 cycles at 1 C. This work offers a viable lattice engineering to address the stability and low initial Coulombic efficiency of the Ni-rich layered oxides, and facilitates the implementation of Li-ion batteries with high-energy density and long durability.

1. Introduction

Anisotropic volume variation is an intrinsic disadvantage of layered cathodic oxides because of the insertion and extraction of interlaminar ions during cycling.[1–4] In detail, the lattice changes along axis *a*(*b*) are small, while those along axis *c* are large. This heterogeneous volume change (especially during the H2-H3 phase change process) in Ni-rich cathode materials leads to crystal structure fatigue (including distorted lattice and formation of cracks) that renders the active material ineffective.[5–8] Thus, suppressing the volume change in Ni-rich materials is vital importance for durable batteries. Modified strategies such as doping or coating can partially conquer this issue,[7–10] but the evolution of intrinsically anisotropic lattice parameters in layered oxides is inevitable. It has been recently proven that perovskite phase rivet and high-entropy oxides can significantly alleviate the volume change and thereby stabilized the Ni-rich cathode.[11,12] Despite these advances, it remains challenging and daunting to effectively regulate the detrimental anisotropic volume change and simultaneously achieve a high capacity.

In addition to volume variations during battery operation, another universal drawback of Ni-rich layered materials is that they exhibit a large first-cycle specific capacity loss (12–30%).[13–17] Such a large capacity loss leads to a low initial Coulombic efficiency (ICE), which was raised by the Nobel Laureate M. Stanley Whittingham recently.[18] The main reason for the first-cycle issue can be attributed to the sluggish Li^+ diffusion in the bulk materials, especially at the end of the discharge process.[18–20] It is widely recognized that a high Ni-content or high voltage can enhance the specific capacity, but accompanied by a trade-off of stability.[21–23] Thus, eliminating the large first-cycle capacity loss is an effective way to resolve the stability-capacity dilemma of Ni-contained cathodes. However, up to date, there is no effective strategy to avoid the large first cycle capacity

---

X. Tan, Z. Chen, M. Zhang, S. Li, F. Pan
School of Advanced Materials
Peking University
Shenzhen Graduate School
Shenzhen 518055, China
E-mail: panfeng@pkusz.edu.cn

X. Tan, Y. Zhang, W. Chu
Nanofabrication Laboratory
CAS Key Laboratory for Nanophotonic Materials and Devices
National Center for Nanoscience and Technology
Beijing 100190, China
E-mail: wgchu@nanoctr.cn

T. Liu
Chemical Sciences and Engineering Division
Argonne National Laboratory
Lemont, IL 60439, USA

K. Liu, P. Yang
The Institute of Technological Sciences
MOE Key Laboratory of Hydrodynamic Transients
Wuhan University
Wuhan 430072, China
E-mail: peihua.yang@whu.edu.cn

The ORCID identification number(s) for the author(s) of this article can be found under https://doi.org/10.1002/adma.202301096

DOI: 10.1002/adma.202301096

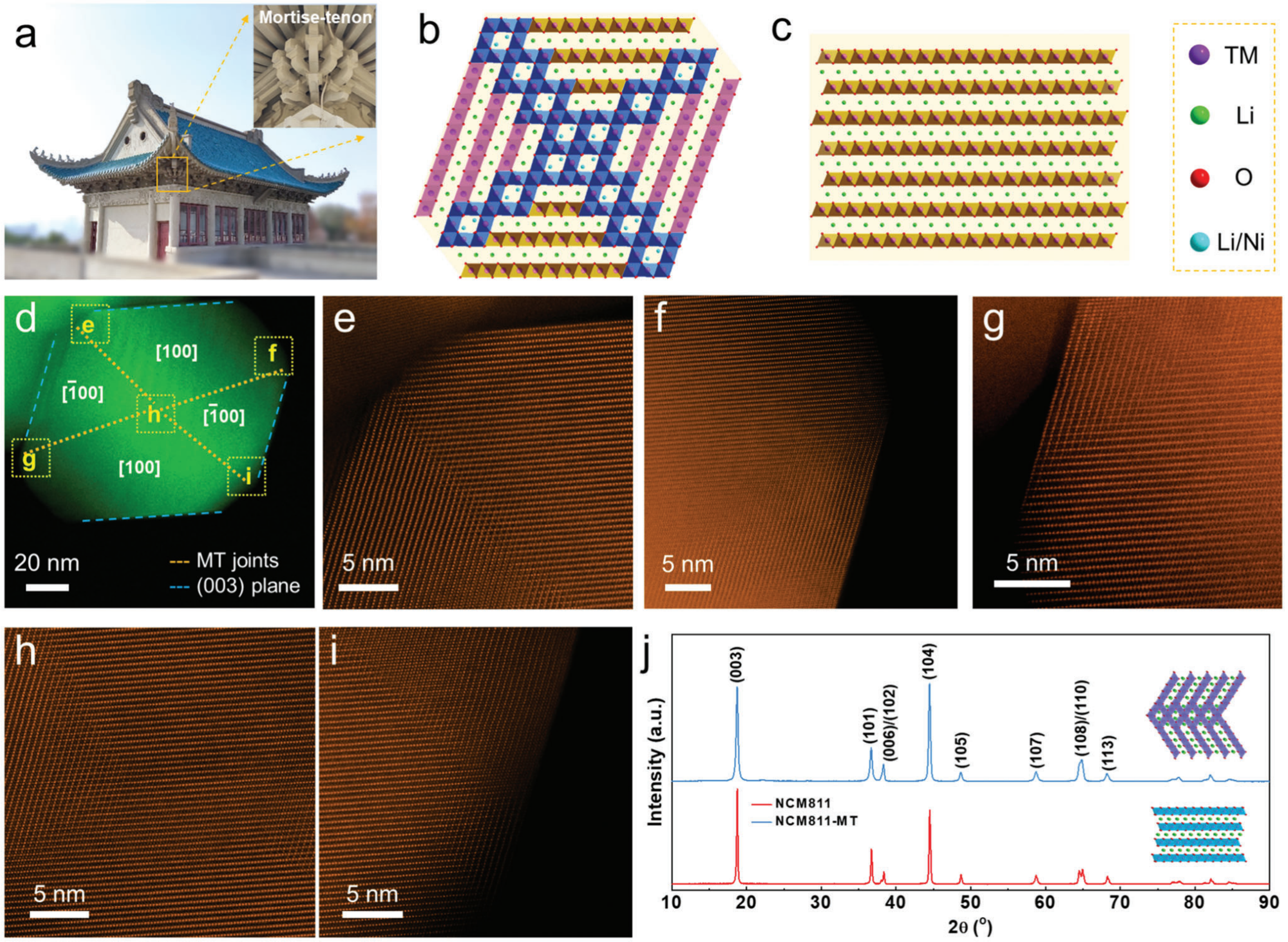

Figure 1. Illustration and characterizations of MT structures. a) MT structure in a traditional Chinese building (Cherry Garden, Wuhan University). b,c) Schematic of particles with coupled MT structures (b) and with a plain layered structure (c). Blue, pink, and orange octahedra represent spinel MT structure in [110] axis, layered structure in [$\bar{1}$00] axis and layered structure in [100] axis, respectively. d) HAADF image of a NCM811-MT particle. e–i) Atomically resolved HAADF STEM images at the five locations marked in (d). j) XRD patterns of NCM811 and NCM811-MT.

loss. The above-mentioned volume variation and sluggish ion diffusion can all be traced to structural drawbacks; thus, structural engineering is expected to be the most effective and straightforward way to improve the electrochemical performance of the Ni-rich layered materials.

Inspired by the robust mortise-tenon joints in traditional Chinese buildings, we design and fabricate layered $LiNi_{0.8}C_{0.1}Mn_{0.1}O_2$ with spinel-like mortise-tenon structures (NCM811-MT). Like logs in the architectural MT joints for a perfect connection, the layers of NCM811 are wedged into each other through the jagged ends at the spinel-like MT zones. The advantages of layered materials with such structure are summarized as follows. First, the MT structure is strain-retardant to prevent the volume variations. Second, the MT structure can provide an expressway for fast lithium-ion transport. Third, the MT structure in layered materials results in most of the particle surfaces being terminated by the stable (003) lattice planes. These superiorities are evidenced by extensive experimental and simulation data, and contribute to the significantly enhanced cycling stability and ICE of NCM811-MT. This architectural MT design broadens the insights for stable crystal structures and paves the way for developing advanced and durable batteries with high energy densities through structural engineering.

2. Results and Discussion

Figure 1a shows a typical MT structure in a traditional Chinese building, which can survive more than hundreds of years.[24,25] The crystallographic schematics of coupled MT structures and a plain layered structure are displayed in Figure 1b,c, respectively, which are also magnified in Figure S1 (Supporting Information) for better clarity. Both high resolution transmission electron microscopy (HRTEM) images and selected area electron diffraction (SAED) patterns reveal that the NCM811 exhibits typical layered crystalline structure in space group $R\bar{3}m$ (Figure S2, Supporting Information). The aberration-corrected high-angle annular dark-field scanning transmission electron microscope (HAADF-STEM) images of a NCM811-MT particle are presented in Figure 1d–i. The MT joints separate the whole particle into four domains with the adjacent areas are [100] and [$\bar{1}$00] zone axis

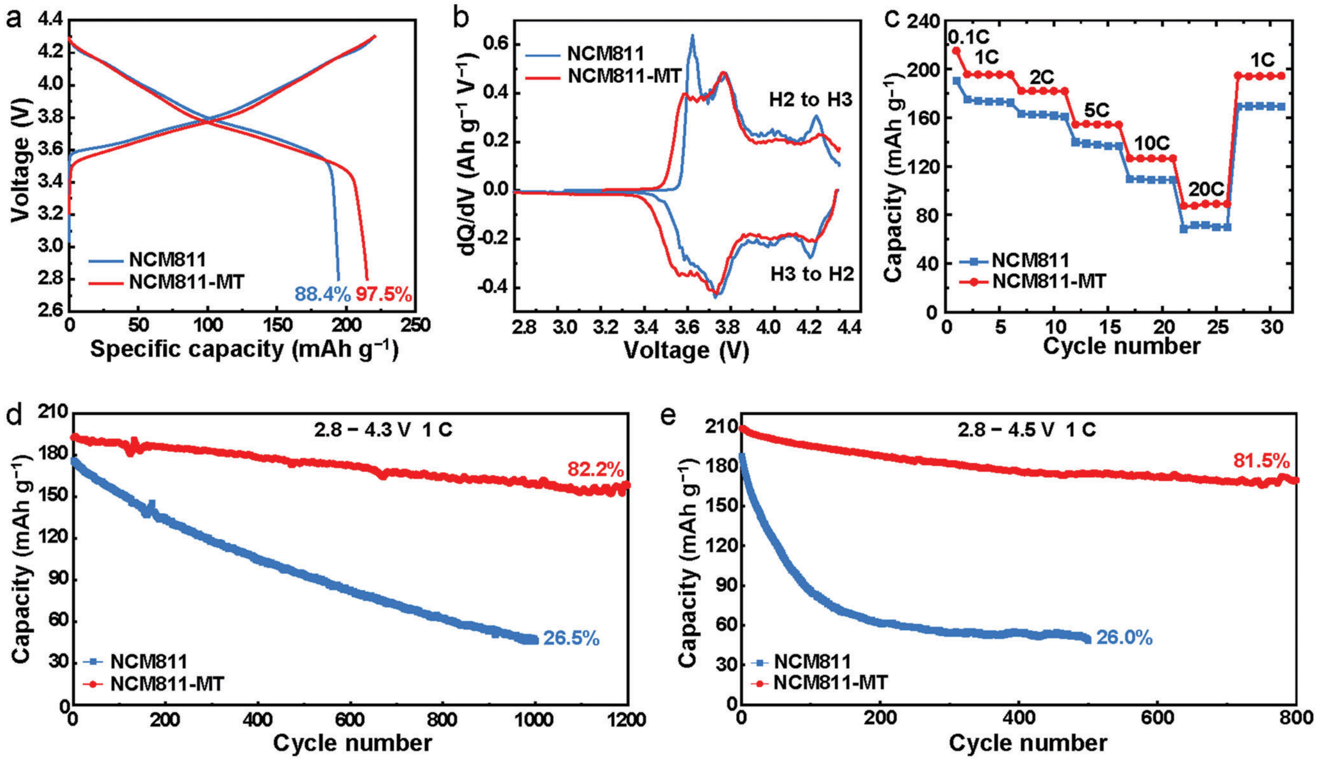

Figure 2. Electrochemical performance of the NCM811 and NCM811-MT. a) Initial charge–discharge profiles at the current of 0.1 C. b) The corresponding differential capacity (dQ/dV) curves. c) Rate performance. d–e) Cycling performance.

alternately. The adjacent (003) planes tilt ≈109.5° or 70.5°, which are coherent with the spinel-like MT structure. Consequently, rational merging these domains together creates a spinel-like MT structure and a stable (003) surface-dominated particle (Figures S3–S5, Supporting Information). For better understanding, the complex SAED pattern in Figure S3 (Supporting Information) was elaborated in Figure S6 (Supporting Information). While the average particle size of NCM811-MT reduced to 93 nm (155 nm for NCM811) after the introduction of Li_2SO_4, the particles were more angular (Figure S7, Supporting Information).

In addition to the local morphology investigation, the X-ray powder diffraction (XRD) was conducted to study the ensemble averaged crystal structure of the particles (Figure 1j; Figure S8, Supporting Information). All the evident peaks can be indexed to a typical α-$NaFeO_2$ layered structure in the space group $R\bar{3}m$. Rietveld refinements were conducted, and the results were listed in Table S1 (Supporting Information). The lattice parameter c (a) is decreased (increased) from 14.191 (2.869) Å for NCM811 to 14.181 (2.872) Å for NCM811-MT. Meanwhile, the anti-site rate is similar for the two samples (3.8% for NCM811 and 4.6% for NCM811-MT), thus its impact on the lattice is insignificant.[26,27] The (003) d-spacing of the layered structure is larger than the (111) d-spacing of the spinel structure, and this lattice change indicates the formation of spinel structures in NCM811-MT.[28] The grain size of NCM811 and NCM811-MT is calculated to be 117.2 (1.7) and 24.3 (0.2) nm, respectively. Taking the particle size into account, the ratio of grain size/average particle size is 75% and 26% for NCM811 and NCM811-MT, which implies that the NCM811-MT particle consists of multiple grains.

It is worth noting that trace Li_2SO_4 can still be detected in NCM811-MT (Figure S8c, Supporting Information), which is also confirmed by the spectra of X-ray photoelectron spectroscopy (XPS, Figure S9, Supporting Information), suggesting that Li_2SO_4 is very stable and does not react with the materials at high temperatures.[29] The Li_2SO_4 was quantified to be 2.14 wt.% (molar ratio is 1.91%) in the NCM811-MT product by a carbon–sulfur analyzer. The spinel-like MT structures are formed during the process of "welding" small particles into a larger one (Figure S10, Supporting Information), and Li_2SO_4 is uniformly distributed in the material during synthesis (Figure S11, Supporting Information). It is speculated that Li_2SO_4 can transport ions to build the spinel-like MT joint zone at high temperatures.[30] To further investigate the possible formation mechanism of MT structures, we synthesized NCM811 with Na_2SO_4 or Li_3PO_4 as the additive. As results, spinel-like MT structures are observed in the final products (Figure S12, Supporting Information). Indeed, spinel structures can form on the surface of lithium-rich layered oxides when polyanions are introduced during synthesis.[31] Thus, polyanions such as SO_4^{2-} and PO_4^{3-} play a key role in the formation of spinel-like structures. The formation process of the spinel-like MT structures is summarized and presented in Figure S13 (Supporting Information).

The detailed crystalline structures determine the ion storage properties of the layered materials. The initial charge–discharge curves of NCM811-MT and NCM811 at 0.1 C (1 C = 280 mA g^{-1}) are compared in **Figure 2**a. With a similar charge capacity of ≈220 mAh g^{-1}, NCM811-MT and NCM811 presents a discharge capacity of 215 and 195 mAh g^{-1}, respectively. The ICE of

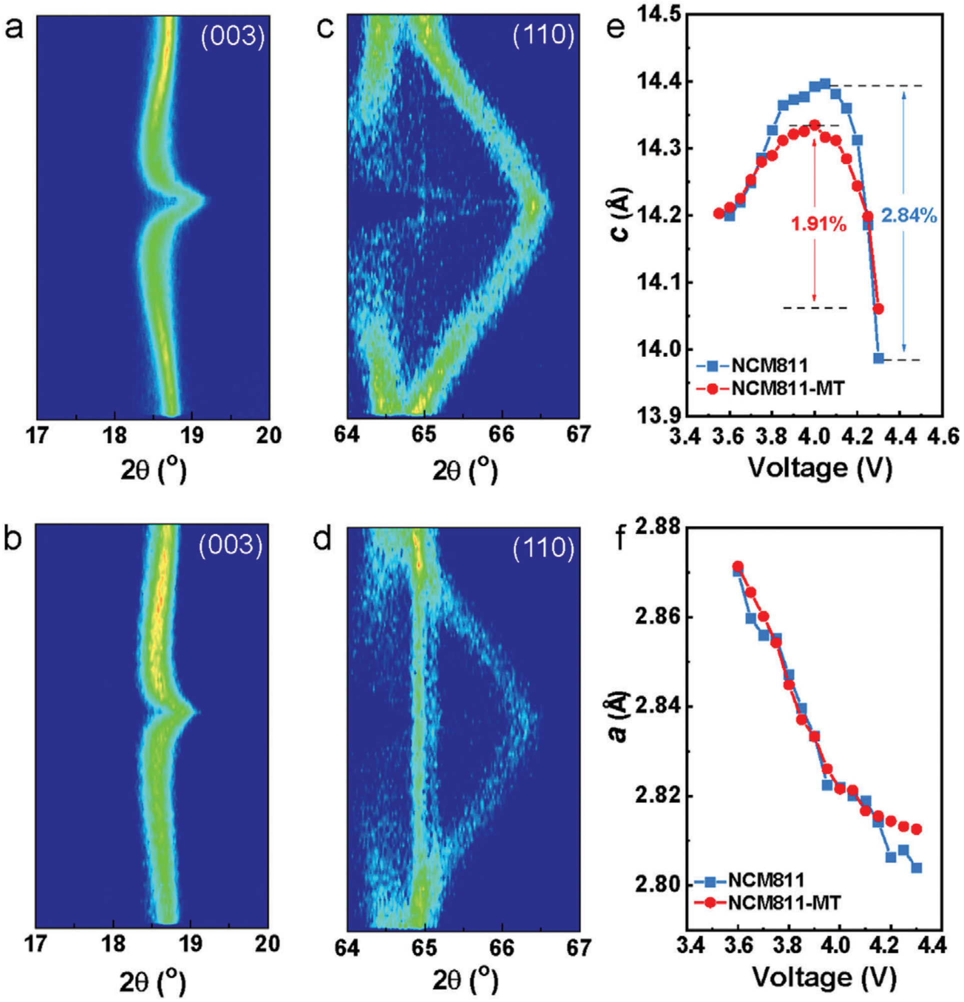

Figure 3. Structural evolution during the first charge–discharge process. Contour plot of a) the (003) and c) the (110) reflection of NCM811. Contour plot of b) the (003) and d) the (110) reflection of NCM811-MT. e,f) Lattice parameter of *c* and *a* as functions of voltage.

NCM811-MT reaches 97.5%, which is much higher than that of NCM811 (88.4%). The dQ/dV curves in Figure 2b reveal that the detrimental H2-H3 phase transition was suppressed in NCM811-MT, which is consistence with the cyclic voltammetry (CV) results (Figure S14, Supporting Information). The pair of redox peaks at ≈3.1 V may be attributed to the capacity contribution of spinel structure in NCM811-MT.[12] The much lower initial capacity loss at different cut-off voltages (Figure S15, Supporting Information) confirms that the long-standing inherent kinetics limitation (in the low voltage range during discharging) of Ni-rich layered material was overcome in NCM811-MT.[14,18,19]

NCM811-MT exhibits higher capacities than that of NCM811 at various rates (Figure 2c), implying that the MT structures can enable superior rate capabilities. The capacity retention after 1200 cycles with a voltage range of 2.8–4.3 V for NCM811-MT is 82.2%, which is considerably higher than that of NCM811 (26.5% of 1000 cycles) (Figure 2d). When the cut-off voltage was further increased to 4.5 V, the NCM811-MT still exhibits capacity retention of 81.5% after 800 cycles, which obviously outranges NCM811 cell (Figure 2e). The charge/discharge and dQ/dV profiles during cycling reveal a considerably suppressed internal resistance drop[32] and improved structural reversibility in NCM811-MT (Figures S16 and S17, Supporting Information). It should be noted that the cycling stability of NCM811-MT (state-of-the-art) is much higher than recently reported single crystal[33] and core-shell microstructured Ni-rich materials,[34] and the details of performance comparison is shown in Table S2 (Supporting Information).

To reveal the function of the spinel-like MT structure in the cathode, we conducted in situ XRD to study the volume change and phase evolution during the charge/discharge process. The cells were tested at 2.8–4.3 V at a current of 0.1 C. In the XRD pattern of hexagonal layered structure NCM811, the position changes of (003) peak indicate the variation of *c* value, while (110) represents the variation of *a* value.[35] In general, during de-lithiation/lithiation of NCM811, the *c* value changes significantly, while the *a* value changes slightly. The contour maps of (003) and (110) reflections of the two samples are summarized in **Figure 3**, according to the recorded patterns in Figure S18 (Supporting Information). While the (003) peak initial mild shift to low angle followed by a sudden shift to high angle during charging for both of the samples, and vice versa during discharging

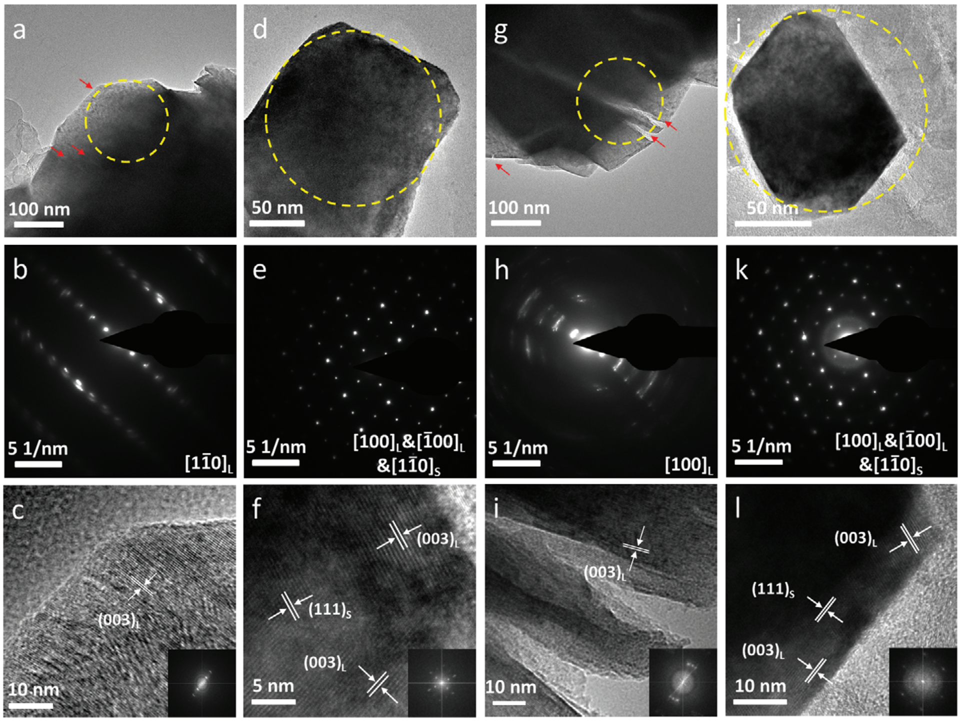

Figure 4. Morphological and structural evolution of the cathode materials after 500 cycles with cutoff voltages of a–f) 4.3 V and g–l) 4.5 V at 1 C. a–c) and g–i) TEM images, corresponding SAED patterns and HRTEM images of NCM811. d–f) and j–l) TEM images, corresponding SAED patterns and HRTEM images of NCM811-MT. The selected areas for electron diffraction are marked by dash circles in (a,d,g,j). The subscripts L and S indicate layered and spinel structures, respectively.

(Figure 3a,b). The (003) peak variation of NCM811-MT was 0.32°, which is much lower than 0.57° for NCM811. The variation of (110) during charging for NCM811-MT and NCM811 was 1.34° and 1.53°, respectively (Figure 3c,d). The calculated *c*-axis lattice parameters variation is less pronounced in NCM811-MT compared to that of NCM811, with a maximum Δc of 1.91% (vs 2.84% for NCM811) (Figure 3e). The maximum Δa is similar but the difference tends to be slighter, which was 2.05% and 2.31% for NCM811-MT and NCM811, respectively (Figure 3f). As a result, the volume change was significantly limited in NCM811-MT. The less significant volume change of NCM811-MT relative to NCM811 can be associated with the spinel-like MT structure, which constructs a robust connection between the unconsolidated layers along *c* and the rigid lattice along *a*.

We further investigated the structural and interfacial evolutions of the cathodic materials after long-term cycles using TEM. The emerging of microcracks and surface degradation were observed in the cycled NCM811 (**Figure** 4a–c; Figure S19, Supporting Information), which is similar to previous results.[36] As confirmed by the SEAD pattern (Figure 4b) and HRTEM images (Figure 4c), large area distortion was observed in the NCM811 after cycling. In sharp contrast, no structural distortion was observed in cycled NCM811-MT, and the surface degradation was quite limited (Figure 4d–f; Figure S20, Supporting Information). More severe structure degradations are expected when further increasing the cut-off voltage to 4.5 V,[37] and obvious cracks and severe lattice distortions were observed in NCM811 (Figure 4g–i; Figure S21, Supporting Information). No rock-salt phases formed in NCM811 at 4.5 V could be related to the rapidly growing overpotential (Figures S16 and S17, Supporting Information), which blocks lithium de-lithiation. The residual Li acts as an immense obstacle to the phase transition toward rock-salt.[38] However, the NCM811-MT was still stable, without any distortions and cracks formed in the lattice (Figure 4j–l; Figure S22, Supporting Information). Besides, the spinel-like MT and layered structures in NCM811-MT were well preserved and have not transformed into rock-salt phase, as proved by the HRTEM images (Figure 4l; Figure S22, Supporting Information). It can be inferred that, the spinel-like MT structure presents a strain-retardant function, which is beneficial to enhance structural stability of NCM811-MT.[11] The improved surface stability of NCM811-MT can be ascribed to its dominated (003) surface.[39–41]

To further understand the diffusion kinetics of lithium ions, we conducted electrochemical impedance spectroscopy (EIS) of the two cells at different cycles (Figure S23, Supporting Information). The equivalent circuit consists of solid electrolyte interface resistance (R_{SEI}, high-frequency range semicircle), charge transfer resistance (R_{ct}, medium-frequency range semicircle), and Warburg-type element reflecting the diffusion of $\mathrm{Li^+}$ in cathode materials (low-frequency tail).[42] Considerable R_{ct} increment was observed upon cycling for NCM811, which increased from 14.8 Ω (1st) to 486.7 Ω (500th). In contrast, the R_{ct} of NCM811-MT increased slightly from 2.4 to 44.4 Ω after 500 cycles (Figure S23c, Supporting Information), implying fewer side reactions happen. Furthermore, the Li-ion diffusion coefficient ($D_{\mathrm{Li+}}$) of NCM811-MT remains almost constant during cycling ($\approx 3 \times 10^{-10}$ cm^2 s^{-1}), while such parameter in NCM811 is reduced by an order of magnitude after only 300 cycles (from

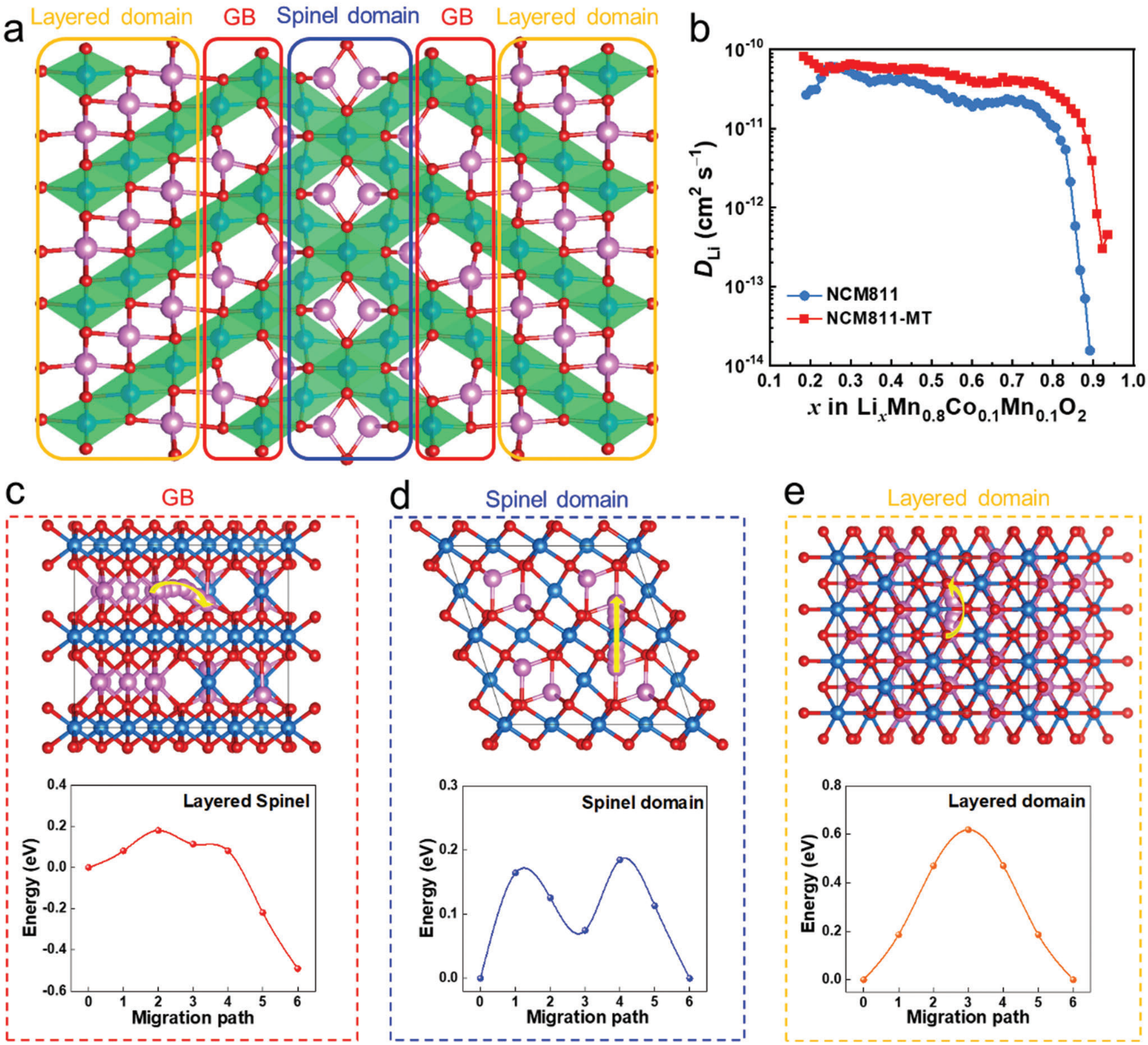

Figure 5. Fast lithium-ion diffusion in NCM811-MT. a) Schematic of the spinel, layered domain and their boundaries. b) Lithium-ion diffusion coefficient by GITT. c–e) Lithium-ion diffusion energy barrier c) at the GB, d) within the spinel, and e) in the layered domain.

≈3 × 10^{-10} to ≈3 × 10^{-11} cm^2 s^{-1}) (Figure S23d, Supporting Information). Due to the spinel-like MT structure, NCM811-MT exhibits a not only higher initial value but stable Li-ion diffusion coefficient than that of NCM811, indicating a well-maintained structure, which is consistent with the TEM.

The enhanced ICE and rate performance of the NCM811-MT is considered to be closely related to the inborn spinel-like MT structure. To elaborate on how the MT structure impacts the Li ions transport, lithium-ion diffusions barriers at the grain boundary (GB), in the spinel domain and the layered domain have been calculated. The model of highly symmetrical layered structures connected by a spinel-like MT is displayed in **Figure 5**a. The lithium-ion diffusion energy barriers oblique to the GB and within the spinel structure is 0.18 and 0.19 eV (Figure 5c,d), respectively. Both of the values are much lower than that in the layered structure (0.62 eV, Figure 5e). According to the Arrhenius relationship, the decrease of the energy barrier can significantly facilitate the ionic diffusion.[43] Therefore, a spinel-like MT structure implanted in the layered structure is an expressway for lithium-ion transport in the bulk materials. To verify the calculation results, the lithium-ion diffusion coefficient based on the galvanostatic intermittent titration technique (GITT) of the cathodic materials with and without spinel-like MT was conducted (Figure 5b). It should be noted that the ion diffusion coefficient values are slightly different in GITT and EIS due to the different measurement principles. The measured $D_{\mathrm{Li}+}$ of NCM811-MT is obviously higher than that of NCM811, especially with high lithium content (Figure 5b). Therefore, it can be concluded that, due to the implantation of spinel-like MT structures, the intrinsic slow lithium kinetics plague of NCM811 at the high lithium contents is overcome.

3. Conclusion

In summary, we propose and synthesize Ni-rich layered $LiNi_{0.8}Co_{0.1}Mn_{0.1}O_2$ materials with implanted spinel-like MT structures. The MT structures not only improve the mechanochemical stability by suppressing the intrinsic anisotropic volume change, but also provide an expressway for fast Li-ion transport. In addition, due to the formation of MT structures, the NCM particles are extensively terminated with the most stable (003) planes, which can mitigate the cathode–electrolyte interfacial reactions. As a consequence, NCM811-MT exhibits quite excellent electrochemical properties with a capacity retention of 82.2% after 1200 cycles at 1 C and a high initial Coulombic efficiency of 97.5% at 0.1 C. This new lattice engineering strategy, introducing robust spinel-like MT structures into the layered oxides, may shed light on the design of Ni-rich layered cathodes with high structural stability and negligible first-cycle capacity loss.

4. Experimental Section

Synthesis of $LiNi_{0.8}Co_{0.1}Mn_{0.1}O_2$ with Spinel-Like Mortise-Tenon Structure (NCM811-MT): The materials were prepared by a sol–gel method. Stoichiometric amounts of lithium nitrate (Macklin, 99.9%), nickel nitrate hexahydrate (Aladdin, AR, 98%), cobalt nitrate hexahydrate (Aladdin, AR, 99%), and manganese nitrate (Macklin, AR, 50 wt.% in H_2O) were mixed with citric acid (Macklin, 99.5%) and lithium sulfate (Macklin, 99%) in 200 mL deionized water (total transition metals: 0.08 mol). The molar ratios of citric acid to the total metal ions and sulfate to transition metals were 1:4 and 2:100, respectively. After magnetic stirring overnight, the solution was dried at 80 °C to form gel, which was subsequently heated at 230 °C for 5 h and then ground well to form the precursor. The precursor (5 g each time) was calcined at 550 °C for 4 h and 750 °C for 15 h in oxygen. In comparison, $LiNi_{0.8}Co_{0.1}Mn_{0.1}O_2$ (NCM811) was also synthesized by the same method without adding lithium sulfate.

Materials Characterizations: The crystallographic structure of samples was identified by power X-ray diffraction (XRD, Bruker D8-Advance diffractometer) at a step mode with 0.02° per step and a sampling time of 1 s, using Cu-Kα radiation at 40 kV and 80 mA. The in situ XRD tests were performed on the same instrument using an in situ XRD cell in the 2θ angular range of 15–70° at a scan rate of 5° min^{-1}. FullProf program was employed for the XRD Rietveld refinements. The morphology and microstructure of the samples were characterized by scanning electron microscope (SEM, ZEISS Supra 55 field emission SEM) and high-resolution field-emission transmission electron microscopy (FETEM, JEOL-3200FS, 300 kV). The cycled cell (fully discharged) was disassembled to get the cathode, which was washed by DMC for five times and immersed in NMP (sealed in a tube) in an argon filled glove box. To obtain the dispersive particles for TEM observation, the tube with a cathode inside was ultrasonically treated for 30 min. The air exposure time of the cycled particles was <10 min, before TEM observation. TEM coupled with energy dispersive X-ray spectrometry (EDS) was used to detect the elemental distribution. XPS with the excitation energy of 1486.68 eV (Al Kα source) was used to analyze the chemical state and composition. The atomic structure of the samples was acquired on a high-angle annular dark-field scanning transmission electron microscope (HAADF-STEM, JEM-AEM300F, Japan) operated at 300 kV and equipped with double spherical aberration correctors. The element analysis and etching profiles were acquired on an ESCALab 250Xi electron spectrometer. Carbon–sulfur analyzer (Horiba EMIA-8100, Contrinex, Germany) was used to determine the content of S in the final product.

Electrochemical Measurements: Electrochemical properties were evaluated using coin cells (CR2032) assembled in an argon filled glove box. To fabricate the working electrodes, 80 wt.% active materials, 10 wt.% polyvinylidene fluoride (PVDF), and 10 wt.% acetylene black were mixed in N-methyl pyrrolidone (NMP) solvent, followed by cast the slurry onto the aluminum foil and dried at 100 °C overnight in a vacuum oven. The mass loading of the active materials was ≈2 mg cm^{-2}. Metal Li and Celgard 2316 were used as the anode and separator, respectively. The electrolyte was 1 M $LiPF_6$ dissolved in a 1:1:1 volume ratio of ethylene carbonate: ethyl methyl carbonate: dimethyl carbonate, with a 5% vinylene carbonate additive. Galvanostatic charge–discharge and galvanostatic intermittent titration technique (GITT, charging/discharging and waiting time was 10 min and 1 h, respectively) measurements were carried out on a Neware battery test system (CT-4008T-5V10mA-164, Shenzhen, China) at room temperature (≈25 °C). Cyclic voltammetry (CV) and electrochemical impedance spectroscopy (EIS) were conducted on a Solartron electrochemical workstation. The cells were charged to 4.3 V before the EIS tests (100 kHz to 0.01 Hz with an AC oscillation amplitude of 5 mV for measurement).

First Principles Calculations: The Vienna Ab initio Simulation Package (VASP) with a plane-wave basis set[44] and the projector-augmented wave pseudopotentials[45] were used to perform density functional theory (DFT) calculations with a plane-wave cutoff energy of 520 eV. The spin-polarized generalized gradient approximation (GGA) with Perdew–Burke–Ernzerhof (PBE) function was used to treat the exchange-correlation effects.[46] To correctly characterize the localized electronic states of the transition metal oxide materials, the GGA+U method was used.[47] The U value for the Ni 3d state was chosen to be 6.4 eV.[48] The Monkhorst-Pack *k*-point grid[49] with a total number of at least 1000/(the number of atoms per cell) points for all directions, was used for the integration in the Brillouin zone. The convergence tolerance for residual force on each atom during structure relaxation was 0.02 eV Å^{-1}. The convergence criterion of force was 0.05 eV Å^{-1}.[50]

Supporting Information

Supporting Information is available from the Wiley Online Library or from the author.

Acknowledgements

X.T. and Z.C. contributed equally to this work. This work was financially supported by the China Postdoctoral Science Foundation (2022M720207), the National Natural Science Foundation of China (22209124), startup funding of Wuhan University, the Strategic Priority Research Program of the Chinese Academy of Sciences (no. XDB36000000), the Soft Science Research Project of Guangdong Province (no. 2017B030301013), the Shenzhen Science and Technology Research (JCYJ20200109140416788), the Basic, Applied Basic Research Foundation of Guangdong Province (no. 2021B1515130002), the National Natural Science Foundation of China (52172175), and the Shenzhen Science and Technology Research Grant (JCYJ20210324130812033 and JCYJ20200109140416788). This work was also supported from Clean Vehicles, the US-China Clean Energy Research Centre (CERC-CVC2) under US DOE EERE Vehicle Technologies Office. Argonne National Laboratory is operated for DOE Office of Science by the UChicago Argonne, LLC, under contract number DE-AC02-06CH11357.

Conflict of Interest

The authors declare no conflict of interest.

Data Availability Statement

The data that support the findings of this study are available from the corresponding author upon reasonable request.

Keywords

fast lithium-ion transport, initial Coulombic efficiency, mortise-tenon structures, Ni-rich layered cathodes, volume variations

Received: February 4, 2023
Revised: March 28, 2023
Published online: June 30, 2023

---

[1] Y. Bi, J. Tao, Y. Wu, L. Li, Y. Xu, E. Hu, B. Wu, J. Hu, C. Wang, J.-G. Zhang, Y. Qi, J. Xiao, *Science* **2020**, *370*, 1313.
[2] J. Li, C. Lin, M. Weng, Y. Qiu, P. Chen, K. Yang, W. Huang, Y. Hong, J. Li, M. Zhang, C. Dong, W. Zhao, Z. Xu, X. Wang, K. Xu, J. Sun, F. Pan, *Nat. Nanotechnol.* **2021**, *16*, 599.
[3] L. Wang, X. Lei, T. Liu, A. Dai, D. Su, K. Amine, J. Lu, T. Wu, *Adv. Mater.* **2022**, *34*, 2200744.
[4] L. de Biasi, B. Schwarz, T. Brezesinski, P. Hartmann, J. Janek, H. Ehrenberg, *Adv. Mater.* **2019**, *31*, 1900985.
[5] S. Zhang, J. Ma, Z. Hu, G. Cui, L. Chen, *Chem. Mater.* **2019**, *31*, 6033.
[6] H. H. Sun, H.-H. Ryu, U.-H. Kim, J. A. Weeks, A. Heller, Y.-K. Sun, C. B. Mullins, *ACS Energy Lett.* **2020**, *5*, 1136.
[7] L. Ni, S. Zhang, A. Di, W. Deng, G. Zou, H. Hou, X. Ji, *Adv. Energy Mater.* **2022**, *12*, 2201510.
[8] X. Fan, X. Ou, W. Zhao, Y. Liu, B. Zhang, J. Zhang, L. Zou, L. Seidl, Y. Li, G. Hu, C. Battaglia, Y. Yang, *Nat. Commun.* **2021**, *12*, 5320.
[9] P. Oh, J. Yun, S. Park, G. Nam, M. Liu, J. Cho, *Adv. Energy Mater.* **2020**, *11*, 2003197.
[10] C. M. Julien, A. Mauger, *Energies* **2020**, *13*, 6363.
[11] L. Wang, T. Liu, T. Wu, J. Lu, *Nature* **2022**, *611*, 61.
[12] R. Zhang, C. Wang, P. Zou, R. Lin, L. Ma, L. Yin, T. Li, W. Xu, H. Jia, Q. Li, S. Sainio, K. Kisslinger, S. E. Trask, S. N. Ehrlich, Y. Yang, A. M. Kiss, M. Ge, B. J. Polzin, S. J. Lee, W. Xu, Y. Ren, H. L. Xin, *Nature* **2022**, *610*, 67.
[13] S.-H. Kang, W.-S. Yoon, K.-W. Nam, X.-Q. Yang, D. P. Abraham, *J. Mater. Sci.* **2008**, *43*, 4701.
[14] J. Kasnatscheew, M. Evertz, B. Streipert, R. Wagner, R. Klopsch, B. Vortmann, H. Hahn, S. Nowak, M. Amereller, A. C. Gentschev, P. Lamp, M. Winter, *Phys. Chem. Chem. Phys.* **2016**, *18*, 3956.
[15] S. H. Song, M. Cho, I. Park, J. G. Yoo, K. T. Ko, J. Hong, J. Kim, S. K. Jung, M. Avdeev, S. Ji, S. Lee, J. Bang, H. Kim, *Adv. Energy Mater.* **2020**, *10*, 2000521.
[16] W. Zhao, J. Zheng, L. Zou, H. Jia, B. Liu, H. Wang, M. H. Engelhard, C. Wang, W. Xu, Y. Yang, J. G. Zhang, *Adv. Energy Mater.* **2018**, *8*, 1800297.
[17] L. Ni, H. Chen, W. Deng, B. Wang, J. Chen, Y. Mei, G. Zou, H. Hou, R. Guo, J. Xie, X. Ji, *Adv. Energy Mater.* **2022**, *12*, 2103757.
[18] H. Zhou, F. Xin, B. Pei, M. S. Whittingham, *ACS Energy Lett.* **2019**, *4*, 1902.
[19] C. Hong, Q. Leng, J. Zhu, S. Zheng, H. He, Y. Li, R. Liu, J. Wan, Y. Yang, *J. Mater. Chem. A* **2020**, *8*, 8540.
[20] J.-w. Choi, J.-w. Lee, *J. Power Sources* **2016**, *307*, 63.
[21] H.-J. Noh, S. Youn, C. S. Yoon, Y.-K. Sun, *J. Power Sources* **2013**, *233*, 121.
[22] W. Li, H. Y. Asl, Q. Xie, A. Manthiram, *J. Am. Chem. Soc.* **2019**, *141*, 5097.
[23] M. Jeong, W. Lee, S. Yun, W. Choi, H. Park, E. Lee, J. Kim, S. J. Cho, N. H. Lee, H. J. Shin, W. S. Yoon, *Adv. Energy Mater.* **2021**, *12*, 2103052.
[24] Y. Lin, Q. Chun, C. Zhang, Y. Han, H. Fu, *J. Wood Sci.* **2022**, *68*, 1.
[25] Q. Chun, H. Jin, Y. Dong, Y. Hua, Y. Han, *Int. J. Archit. Heritage* **2019**, *14*, 729.
[26] H. He, J. Dong, D. Zhang, D. Hang, X. Zhu, C. Chang, *Int. J. Energy Res.* **2020**, *45*, 7108.
[27] M. J. Zhang, X. Hu, M. Li, Y. Duan, L. Yang, C. Yin, M. Ge, X. Xiao, W. K. Lee, J. Y. P. Ko, K. Amine, Z. Chen, Y. Zhu, E. Dooryhee, J. Bai, F. Pan, F. Wang, *Adv. Energy Mater.* **2019**, *9*, 1901915.
[28] M. G. S. R. Thomas, W. I. F. David, J. B. Goodenough, P. Groves, *Mater. Res. Bull.* **1985**, *20*, 1137.
[29] X. Tan, T. Zhao, L. Song, D. Mao, Y. Zhang, Z. Fan, H. Wang, W. Chu, *Adv. Energy Mater.* **2022**, *12*, 2200008.
[30] R. Tärneberg, A. Lundén, *Solid State Ionics* **1996**, *90*, 209.
[31] Y. Zhao, J. Liu, S. Wang, R. Ji, Q. Xia, Z. Ding, W. Wei, Y. Liu, P. Wang, D. G. Ivey, *Adv. Funct. Mater.* **2016**, *26*, 4760.
[32] X. Tan, L. Guo, S. Liu, J. Wu, T. Zhao, J. Ren, Y. Liu, X. Kang, H. Wang, L. Sun, W. Chu, *Adv. Funct. Mater.* **2019**, *29*, 1903003.
[33] L. Ni, R. Guo, S. Fang, J. Chen, J. Gao, Y. Mei, S. Zhang, W. Deng, G. Zou, H. Hou, X. Ji, *eScience* **2022**, *2*, 116.
[34] Y. Zhang, J. Liu, W. Xu, Y. Lu, H. Ma, F. Cheng, J. Chen, *J. Power Sources* **2022**, *535*, 231445.
[35] H.-H. Ryu, K.-J. Park, C. S. Yoon, Y.-K. Sun, *Chem. Mater.* **2018**, *30*, 1155.
[36] F. Friedrich, B. Strehle, A. T. S. Freiberg, K. Kleiner, S. J. Day, C. Erk, M. Piana, H. A. Gasteiger, *J. Electrochem. Soc.* **2019**, *166*, A3760.
[37] W. Li, X. Liu, Q. Xie, Y. You, M. Chi, A. Manthiram, *Chem. Mater.* **2020**, *32*, 7796.
[38] L. Zou, W. Zhao, Z. Liu, H. Jia, J. Zheng, G. Wang, Y. Yang, J.-G. Zhang, C. Wang, *ACS Energy Lett.* **2018**, *3*, 2433.
[39] S. Sharifi-Asl, F. A. Soto, A. Nie, Y. Yuan, H. Asayesh-Ardakani, T. Foroozan, V. Yurkiv, B. Song, F. Mashayek, R. F. Klie, K. Amine, J. Lu, P. B. Balbuena, R. Shahbazian-Yassar, *Nano Lett.* **2017**, *17*, 2165.
[40] C. H. Jung, D. H. Kim, D. Eum, K. H. Kim, J. Choi, J. Lee, H. H. Kim, K. Kang, S. H. Hong, *Adv. Funct. Mater.* **2021**, *31*, 2010095.
[41] W. Lu, J. Zhang, J. Xu, X. Wu, L. Chen, *ACS Appl. Mater. Interfaces* **2017**, *9*, 19313.
[42] X. H. Tan, H. Q. Liu, Y. Jiang, G. Y. Liu, Y. J. Guo, H. F. Wang, L. F. Sun, W. G. Chu, *J. Power Sources* **2016**, *328*, 345.
[43] R. Wang, X. Chen, Z. Huang, J. Yang, F. Liu, M. Chu, T. Liu, C. Wang, W. Zhu, S. Li, S. Li, J. Zheng, J. Chen, L. He, L. Jin, F. Pan, Y. Xiao, *Nat. Commun.* **2021**, *12*, 3085.
[44] G. Kresse, J. Furthmüller, *Phys. Rev. B* **1996**, *54*, 11169.
[45] P. E. Blochl, *Phys. Rev. B* **1994**, *50*, 17953.
[46] J. P. Perdew, K. Burke, M. Ernzerhof, *Phys. Rev. Lett.* **1996**, *77*, 3865.
[47] S. L. Dudarev, G. A. Botton, S. Y. Savrasov, C. J. Humphreys, A. P. Sutton, *Phys. Rev. B* **1998**, *57*, 1505.
[48] W. Lei, T. Maxisch, G. Ceder, *Phys. Rev. B* **2006**, *73*, 195107.
[49] H. J. Monkhorst, J. D. Pack, *Phys. Rev. B* **1976**, *13*, 5188.
[50] G. Henkelman, B. P. Uberuaga, H. Jónsson, *J. Chem. Phys.* **2000**, *113*, 9901.